Multi-physics modelling of packed bed biomass combustion

Ramin Mehrabian [a,b,*], Ali Shiehnejadhesar [a,b], Robert Scharler [a,b,c], Ingwald Obernberger [a,b,c]

[a] BIOENERGY 2020+ GmbH, Inffeldgasse 21b, 8010 Graz, Austria
[b] Institute for Process and Particle Engineering, Graz University of Technology, Inffeldgasse 21b, 8010 Graz, Austria
[c] BIOS BIOENERGIESYSTEME GmbH, Inffeldgasse 21b, 8010 Graz, Austria

HIGHLIGHTS

- A transient 3D model was developed to simulate fuel bed and freeboard of biomass grate furnaces.
- The intra-particle gradients, the bed shrinkage and variations of the bed porosity are considered.
- Detailed kinetic mechanisms are used for the homogeneous gas phase reactions.
- The results are in a good agreement with experimental data.

ARTICLE INFO

ABSTRACT

A transient 3D model for two main zones, namely the fuel bed and the freeboard, of biomass packed bed combustion systems was developed. It integrates the models for the biomass conversion sub-processes and solves the governing equations for the gas and solid phase and their interactions. The intra-particle gradients are included by considering the biomass particles as thermally thick particles. The shrinkage of the packed bed and the variations of the bed porosity due to the uneven consumption of the fuel are taken into account. Detailed kinetic mechanisms are used for the simulation of homogeneous gas phase reactions. To verify the model and to increase the understanding of packed bed combustion, laboratory-scale fixed-bed batch experiments have been performed in a reactor with 9.5 cm diameter and 10 cm length. The model performance was extensively validated with gas phase measurements (CO, CO_2, CH_4, H_2, H_2O and O_2) above the fuel bed, temperatures at different heights in the bed and in the freeboard, and the propagation rate of reaction front. The simulation results are in a good agreement with the measured values.

© 2014 Elsevier Ltd. All rights reserved.

1. Introduction

Among the applied biomass combustion technologies grate-firing is one of the most widely spread, because it can handle a wide range of fuels of varying quality and moisture contents and requires less fuel pretreatment. However, the bed inhomogeneity due to the inhomogeneity of the biomass fuel and insufficient mixing in the fuel bed, causes non-uniform combustion on the grate. This may reduce the efficiency of the plant and increase the emissions. Dealing with these deficiencies requires an improved understanding of the combustion processes in the fuel bed.

Due to the limited accessibility and inhomogeneity inside the packed bed, it is difficult and complex to obtain information by measurements about the conversion processes in the packed bed. As a result, there are few experimental investigations on packed

bed biomass furnaces which include a complete set of measurements. Ryu et al. [1] measured temperatures, species and mass loss profiles of four different biomass types in a fixed bed under fuel-rich conditions. The combustion of straw in a fixed bed was experimentally investigated by van der Lans et al. [2]. They measured temperatures in the packed bed at different heights and species concentrations above the bed. Porteiro et al. [3,4] measured the propagation rates of the reaction front in a fixed bed combustor.

The review of elaborations on packed bed modelling published in literature shows a broad variety of different model approaches to describe entire packed bed systems. The main distinctive features are homogeneous and heterogeneous models. The difference between them lies in the calculation of the energy equation. In homogeneous models the temperature of the gas and of the solid phase are assumed to be equal and one overall energy balance equation is applied [5,2]. The physical properties which appear as constants in the energy equation are described by their effective values over the entire bed. In heterogeneous models the gas phase and the solid phase have individual energy equations [6–8]. They

* Corresponding author at: Institute for Process and Particle Engineering, Graz University of Technology, Inffeldgasse 21b, 8010 Graz, Austria. Tel.: +43 (0) 316 8739232; fax: +43 (0) 316 8739202.

E-mail address: ramin.mehrabian@bioenergy2020.eu (R. Mehrabian).

Nomenclature

A	pre-exponential factor (s^{-1})		X_∞	molar concentration of gas species at bulk flow ($kmol\ m^{-3}$)
a_{p_i}	acceleration of particle i ($m\ s^{-2}$)			
c_i	biomass pseudo-component contributions (–)			
C_1	permeability (m^2)		*Greek symbols*	
C_2	inertial loss coefficient (m^{-1})		α_i	conversion of each biomass pseudo-component (–)
$\mathcal{D}$	diffusivity ($m^2\ s^{-1}$)		δ	distance (m)
E	activation energy ($kJ\ mol^{-1}$)		δ_{ash}	thickness of ash layer (m)
F	view factor		ϵ	emissivity (–)
$\vec{g}$	gravity ($m\ s^{-2}$)		ϕ	porosity (–)
h	heat transfer coefficient ($W\ m^{-2}\ K^{-1}$)		η	tortuosity (–)
h_m	mass transfer coefficient ($m\ s^{-1}$)		μ	viscosity ($kg\ m^{-1}\ s^{-1}$)
k	kinetic rate constant (s^{-1})		ν	stoichiometric coefficient mass basis (–)
k_c	reaction rate constants, char conversion ($m\ s^{-1}$)		ρ	density ($kg\ m^{-3}$)
m	mass (kg)		σ	Stefan–Boltzmann constant ($W\ m^{-2}\ K^{-4}$)
M_c	molecular weight of carbon ($kg\ kmol^{-1}$)		$\tilde{\tau}$	stress tensor (Pa)
n	mole (–)		ω	mass fraction (–)
NC	number of cells		Ω	stoichiometric ratio of moles of carbon per mole of oxi-dising/gasifying agent in corresponding reaction (–)
NP	number of particles			
Nu	Nusselt number (–)		ψ	number of particles per volume (m^{-3})
p	pressure (Pa)			
Pr	Prandtl number (–)			
q	heat flux ($W\ m^{-2}$)		*Subscripts*	
r	reaction rate ($kg\ s^{-1}$)		0	initial condition
R	universal gas constant ($kJ\ mol^{-1}\ K^{-1}$)		ch	char
Re	Reynolds number (–)		dry	drying
S	surface area (m^2)		e	effective
S_{con}	source term in continuity equation ($kg\ m^{-3}\ s^{-1}$)		f	final condition
$\underline{S}_{s,i}$	species i source term ($kg\ m^{-3}\ s^{-1}$)		g	gas
S_m	momentum source term ($kg\ m^{-2}\ s^{-2}$)		lam	laminar
S_q	energy source term ($J\ m^{-3}\ s^{-1}$)		p	particle
t	time (s)		pyr	pyrolysis
T	temperature (K)		rad	radiation
u	velocity ($m\ s^{-1}$)		$turb$	turbulent
			ϑ	radiation control volume

have different temperatures, and heat and mass transfer between the two phases are described by means of Nusselt and Sherwood correlations. When the temperature difference between the gas and solid is not negligible, which is the case for packed bed combustion, heterogeneous modelling is recommended.

Based on the treatment of the solid phase in the heterogeneous models, they can be classified into continuous models [9–12] and discrete particle models [13–16]. Continuous heterogeneous models treat both phases as if they are distributed continuously over the whole spacial domain. At each point in space both phases exist with distinguished properties. The common restriction of continuous packed bed models is that the intra-particle effects cannot be described sufficiently. Additionally, it is very difficult to model the inter-particle interactions in the packed bed with continuous models. The discrete particle models enhance the packed bed modelling by considering the packed bed as an ensemble of representative particles, where each of these particles undergoes thermal conversion processes. In this way the inter-particle effects, e.g. momentum and energy exchanges, can be fully described.

However, there is a limitation in almost all existing models, with the exception of [11], that they consider the packed bed and the freeboard separately, although there is a strong interaction between them. The conversion of the packed bed provides the temperatures and species as inlet conditions for gas phase modelling. Additionally, the published models are validated only to a certain extent, typically using either propagation rates of the reaction front or species profiles. This can be attributed to the fact that experimental data which include complete sets of measurements

with a detailed information about the boundary conditions are scarce.

The objectives of this paper are to present a fully coupled three-dimensional model for the combustion of biomass packed beds which includes both the freeboard and the packed bed as well as detailed experimental data for model validation. A validated comprehensive single particle model [17] for the combustion of thermally thick biomass particles is applied to model the conversion of particles in the packed bed. The size and the position as well as the conversion state of each particle is determined at every time step. The packed bed shrinkage and local porosity of the bed are calculated in each time step. The interaction between the gas phase and particles is considered by an iterative procedure. The radiative heat transfer between the particles and the walls is updated at the beginning of each time step. With these results, the conservation equations of the entire bed are integrated. The homogeneous gas phase reactions are modelled with a detailed kinetic mechanism, instead of applying global reactions. To validate the coupled packed bed/gas phase model, an experimental setup under known conditions has been simulated and the temperature profiles at different heights in the packed bed and in the freeboard, several species concentrations above the fuel bed as well as the propagation of the reaction front are compared with measurements.

2. Experimental setup

The laboratory-scale reactor is a discontinuously operated pot furnace, see Fig. 1. It consists of a cylindrical retort (height
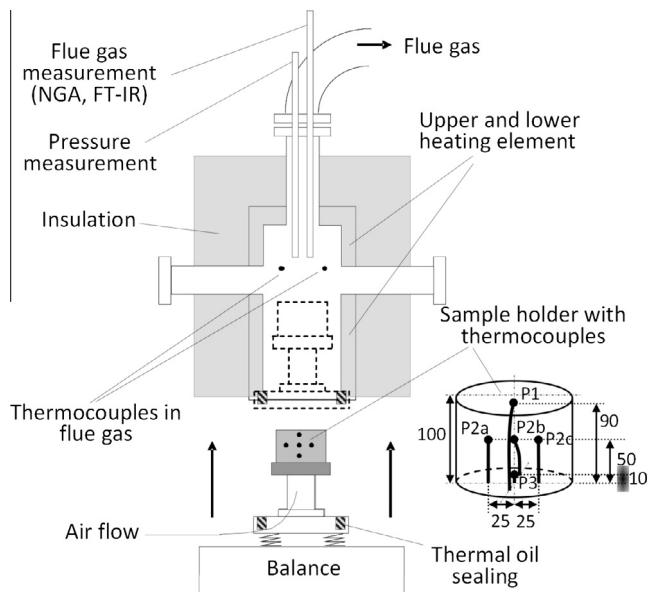
Fig. 1. Scheme of the experimental setup and arrangement of the thermocouples in the fuel bed. Dimensions are in (mm).

0.35 m, i.d. 0.12 m), heated electrically by two separated PID controlled heating circuits. The biomass is put into a cylindrical sample holder (0.100 m height and 0.095 m i.d.) which is located inside the cylindrical retort. The retort and pot are made of fibre-reinforced SiC ceramics. The retort is surrounded by a thick wall of insulated firebricks. The pot rests on a weight balance to measure the mass loss during conversion. Air is introduced through a porous plate at the bottom of the fuel bed. Five thermocouples are installed inside the fuel bed according to Fig. 1. Thermocouples are placed above the sample holder to measure the temperature of the flue gas in the free board. In order to avoid the penetration of false air, the reactor is sealed with thermal oil. The flue gas is extracted from above the fuel bed using a heated suction probe and introduced into an Emerson NGA 2000 to measure O_2 (paramagnetism), CO, CO_2 (NDIR) and H_2 (heat conductivity). Additionally a FT-IR (Ansyco) has been applied to measure H_2O and CH_4. Furthermore, the difference between ambient and reactor pressure is detected for the purpose of correcting the data gained by the weight measurements (causing additional forces acting on the balance). A detailed description of the laboratory-scale reactor was given in previous publications [18].

The experimental conditions for test runs performed and relevant fuel data are summarised in Table 1. The experiment was repeated three times with the same conditions to check the repeatability of the test runs.

3. Methodology

3.1. Particle model

The particle model accounts for intra-particle transport processes and simultaneous sub-processes of thermal conversion of thermally thick solid biomass particles. To reduce the model complexities and calculation time, only the radial temperature gradient in the particle is considered. This is an usual simplification assumption.

To apply the one-dimensional model for a finite cylindrical geometry (as an approximation for the biomass particle shape), Thunman's discretisation [19] approach has been applied. This approach assumes that the particle boundary conditions are homogeneous and every point in the particle at a certain distance from the particle surface has the same temperature and conversion state. The particle is divided into four layers: drying layer, pyrolysis layer, char and ash layer. The boundaries between the layers are related to the conversion sub-processes: drying, pyrolysis and char burnout fronts. At the beginning of the thermal conversion process only drying is of relevance. Due to heating up, moisture starts to get released from the particle. The pyrolysis layer consists of dry biomass and is located around the drying layer as the drying front moves towards the particle centre. When pyrolysis commences, the dry biomass converts to char and volatiles. Volatiles leave the particle and char builds a layer around the pyrolysis layer. Finally, char burnout also creates another layer which contains only ash and surrounds the char layer. As the conversion of the fuel particle proceeds, drying, pyrolysis and char burnout fronts move from the surface to the centre of the particle.

The conversion of each layer is simulated by separate sub-models. It is assumed that drying occurs at a fixed boiling temperature in an infinitely thin zone that separates the wet and the dry part of the particle. The drying process acts as a heat sink, it means that any amount of heat flow above the boiling temperature is consumed by the drying process. It is assumed that there is no resistance to mass transfer, and therefore the water vapour instantaneously leaves the particle. However, the cooling effect of the water vapour transfer through the particle is considered.

Biomass pyrolysis is described by the decomposition of its three pseudo-components hemicellulose, cellulose, and lignin. This model implicitly assumes the hypothesis of an independent decomposition of these three constituents. An Arrhenius equation is used to describe the pyrolysis of each pseudo-component. It represents the dependence of the kinetic rate constant k on the absolute temperature T:

$$k = A \exp\left(-\frac{E}{RT}\right) \tag{1}$$

A is the pre-exponential factor, E is the activation energy and R is the universal gas constant.

The overall mass loss rate of a particle during pyrolysis is given as:

$$-\frac{dm}{dt} = \sum_{i=1}^{3} c_i \frac{d\alpha_i}{dt} \tag{2}$$

where i is related to each pseudo-component, $c_i = m_{0,i} - m_{f,i}$ is a measure of the contribution of the partial decomposition processes to the overall mass loss $m_0 - m_f$. The conversion of each pseudo-component α_i can be expressed by:

Table 1
Experimental conditions and relevant data of the biomass used in the laboratory-scale reactor tests.

Fuel	Oxidising medium	Air flow rate (Nl/min)	Temperature of heated walls		Sample wet mass (g)
			Upper (°C)	Lower (°C)	
Spruce pellets	Air	30	750	450	410
C (wt% d.b.)	H (wt% d.b.)	O (wt% d.b.)	N (wt% d.b.)	Ash (wt% d.b.)	MC (wt% w.b.)
49.5	6.1	44.05	0.05	0.3	7.1

$$\alpha_i = \frac{m_{0,i} - m_i}{m_{0,i} - m_{f,i}} \quad (3)$$

The pseudo-components are all assumed to decompose individually according to a first-order reaction, therefore the conversion rate of each pseudo-component is given by:

$$\frac{d\alpha_i}{dt} = A_i \exp\left(-\frac{E_i}{RT}\right)(1 - \alpha_i) \quad (4)$$

Char conversion models are more complicated than biomass pyrolysis models, as they are based on heterogeneous reactions for which both intrinsic kinetic and transport phenomena are important. Due to the structure of the particle model, the char conversion reactions are assumed to occur at the interface between char and ash layer. Char oxidation with O_2 and gasification with CO_2, H_2O and H_2 are considered as char conversion reactions. The rate of char conversion reactions is a function of both kinetic rate at the reaction surface and mass transfer rate to/from the reaction surface. Assuming a global reaction rate of first order with respect to the oxidising/gasifying agent concentration at the reaction surface, leads to a char conversion rate as:

$$\frac{dm_{ch}}{dt} = -\sum_{i=1}^{4} \frac{\Omega_i M_c}{\frac{1}{k_{c,i}S} + \frac{1}{h_m S} + \int_{\delta_{ash}} \frac{dr}{\mathcal{D}_e S(r)}} X_{\infty,i} \quad (5)$$

where $i = 1$ to 4 corresponds to the heterogeneous reactions in Table 2 and Ω_i is the stoichiometric ratio of moles of carbon per mole of oxidising/gasifying agent in the corresponding reaction. $M_c, S, k_i, \delta_{ash}$ and $X_{\infty,i}$ are the molecular weight of carbon, the surface area of the char burnout front, the kinetic rate constant of heterogeneous reaction i, the thickness of the ash layer and the molar concentration of oxidising/gasifying agent of reaction i in the bulk flow, respectively.

The mass transfer coefficient of reactants in the boundary layer around the particle h_m, is obtained by the Sherwood number. The effective diffusivity of the ash layer $\mathcal{D}_e$, depends on the ash porosity and the molecular diffusivity of the penetrating gaseous component [17].

Since particle shrinkage during drying is much lower compared to that occurring during pyrolysis and charcoal combustion [20], it is postulated that during drying, the size of the particle remains constant and its density decreases. However, both shrinkage and density change during pyrolysis and char burnout are considered in the particle model. The physical properties and parameters used in the particle model are summarised in Table 2. A detailed description of the particle model and its validation are given in [17].

3.2. Bed shrinkage

The consumption of the fuel influences two parameters of the packed bed: one is the shrinkage of the fuel bed and the second one is the bed porosity. Usually it is assumed that the bed continuously shrinks [6–8,26]. However, experimental data show that the shrinkage of the fuel bed is not smooth and the porosity varies within the bed [9]. It may be attributed to uneven fuel consumption across the fuel bed.

One of the main features of the particle model is the calculation of the particle shrinkage during its thermal conversion. It allows to

Table 2
Parameters used in the particle model.

Particle density [21]		
Biomass (wet)	1220	kg m^{-3}
Char	250	kg m^{-3}
Ash	300	kg m^{-3}
Heat capacity [22]		
Biomass	$1500 + T$	J kg^{-1} K^{-1}
Char	$420 + 2.09T - 6.85 \times 10^{-4}T^2$	J kg^{-1} K^{-1}
Ash	$420 + 2.09T - 6.85 \times 10^{-4}T^2$	J kg^{-1} K^{-1}
Thermal conductivity [23]		
Biomass	$0.056 + 2.6 \times 10^{-4}T$	W m^{-1} K^{-1}
Char	0.071	W m^{-1} K^{-1}
Ash	1.2	W m^{-1} K^{-1}
Particle emissivity	$\epsilon = 0.85$	–
Particle size		
Diameter	0.006	m
Length	0.018	m
Pyrolysis model [24]		
	$\mathbf{A} = 2.527 \times 10^{11}$	s^{-1}
Hemicellulose	$\mathbf{E} = 147$	kJ mol^{-1}
	$a = 0.26$	–
	$\mathbf{A} = 1.379 \times 10^{14}$	s^{-1}
Cellulose	$\mathbf{E} = 193$	kJ mol^{-1}
	$a = 0.64$	–
	$\mathbf{A} = 2.202 \times 10^{12}$	s^{-1}
Lignin	$\mathbf{E} = 181$	kJ mol^{-1}
	$a = 0.10$	–
Char conversion model		
Pore diameter	100 [25]	µm
Porosity of ash layer	0.9	
$\Omega C + O_2 \rightarrow 2(\Omega - 1)CO + (2 - \Omega)CO_2$	$k_c = 1.715T \exp(-9000/T)$ [26]	m s^{-1}
	$\Omega = \frac{2[1+4.3\exp(-3390/T)]}{2+4.3\exp(-3390/T)}$ [26]	m s^{-1}
$C + CO_2 \rightarrow 2CO$	$k_c = 3.42T \exp(-15,600/T)$ [26]	m s^{-1}
$C + H_2O \rightarrow CO + H_2$	$k_c = 3.42T \exp(-15,600/T)$ [26]	m s^{-1}
$C + 2H_2 \rightarrow CH_4$	$k_c = 3.42 \times 10^{-3}T \exp(-15,600/T)$ [26]	m s^{-1}

model the shrinkage of the bed based on the shrinkage of individual particles. A UDF is used to calculate the new position of particles. Biomass particles are assumed to be always in contact with beneath particles. Therefore, shrinkage of the bed depends on the fuel conversion. It is assumed that particles can only move in gravity direction. In the UDF for each particle an acceleration is defined as:

$$a_{p_i}^{t+dt} = \frac{u_{p_i}^{t+dt} - u_{p_i}^t}{dt} \tag{6}$$

$$u_{p_i}^{t+dt} = 2\frac{\delta_{p_i,p_{i-1}}^t}{dt} - u_{p_i}^t \tag{7}$$

where $\delta_{p_i,p_{i-1}}^t$ is the distance between particle i and its beneath particle $i-1$. This distance is due to the shrinkage of particles. A loop over all particles is needed, to find the beneath particle of each particle, The particle positions are updated after each execution of the particle model. Therefore, all particles in the packed bed are arranging on their beneath particles to have a compacted bed at the end of each time step. In this way, the uneven fuel consumption in the packed bed causes discontinues shrinkage (bed collapse) and cavities at the surface of the fuel bed.

After having the new position of each particle, the porosity of each cell in the fuel bed is calculated. For this purpose the number of particles in each cell of the fuel bed at current time is needed. Once it is determined, local bed porosity is calculated based on the volume fraction of solid in each computational cell in the fuel bed at every time step.

Hence, the effects of the fuel consumption and the bed shrinkage on the local bed porosity are considered. As it is explained in the next section, the calculated bed porosity is used to determine the gas phase pressure drop in the packed bed.

3.3. Bed pressure loss

The resistance to the gas flow is considered as a source term in the momentum equation of the continuous phase. The source term is calculated using the Ergun equation [27]:

$$\vec{S}_m = -\left(\frac{\mu}{C_1}\vec{u} + C_2\rho_g|u|\vec{u}\right) \tag{8}$$

where μ, u and ρ_g are the viscosity, the gas velocity and the gas density, respectively. The permeability, C_1, and inertial loss coefficient, C_2, for packed beds are functions of the mean particle diameter, d_p, and bed porosity, ϕ:

$$C_1 = \frac{d_p^2\phi^3}{150(1-\phi)^2} \tag{9}$$

$$C_2 = \frac{3.5(1-\phi)}{d_p\phi^3} \tag{10}$$

The grate in the lab-reactor is a screen. It is represented as a uniformly porous medium to consider the resistance to gas flow. To model the pressure loss through a screen or perforated plate the permeability term can be eliminated:

$$\vec{S}_m = -C_2\rho_g|u|\vec{u} \tag{11}$$

The inertial loss coefficient for a screen is tabulated as a function of Reynolds number and free area of the screen in [28].

3.4. Heat transfer

The mathematical description of the heat transfer in the packed bed requires some assumptions and simplifications, due to the

complexity and irregular arrangement of the packed bed. As radiation is the dominant mechanism of heat transfer in combustion systems, the radiative heat transfer has to be considered. It is known that the conduction mechanism is important, if the temperature in the packed bed is below 450 K [29]. Therefore, among the possible conduction routs, only the conduction inside each particle is considered, as it is already explained in the particle model Section 3.1. In addition, gas-particle convective heat transfer is also considered in the calculations. In the following sub-sections the convection and radiation mechanisms are explained.

3.4.1. Convection

In the literature a variety of experimental and theoretical investigations have been published that address the problem of the convective heat transfer in a packed bed. Most of the articles describe a correlation of the mean Nusselt number as a function of the mean Reynolds number. A successful semi-empirical method to calculate the heat transfer rate inside a bed was introduced by [30]:

$$Nu_{lam} = 0.664Pr^{1/3}(Re/\phi)^{1/2} \tag{12}$$

$$Nu_{turb} = \frac{0.037Pr(Re/\phi)^{0.8}}{1 + 2.443(Pr^{2/3} - 1)(Re/\phi)^{-0.1}} \tag{13}$$

$$Nu_p = 2 + \left(Nu_{lam}^2 + Nu_{turb}^2\right)^{1/2} \tag{14}$$

2 in this equation is the asymptotic solution for $Re \to 0$.

Nu_p can now be used to calculate the mean Nusselt number for the packed bed:

$$Nu = f(\phi)Nu_p \tag{15}$$

where $f(\phi)$ is an empirical factor which depends on the porosity of the bed:

$$f(\phi) = 1 + 1.5(1 - \phi) \tag{16}$$

A comparison between the correlations in literature and Eq. (15) is shown in Fig. 2. The empirical correlations from literature depict a scattering of the results due to non-uniformities in the void fraction distributions across the bed which leads to cold by-pass flows as reported by [30,31]. However, the important message of Fig. 2 is that Eq. (15) plausibly correlates the mean Nusselt number to the Reynolds number in packed beds.
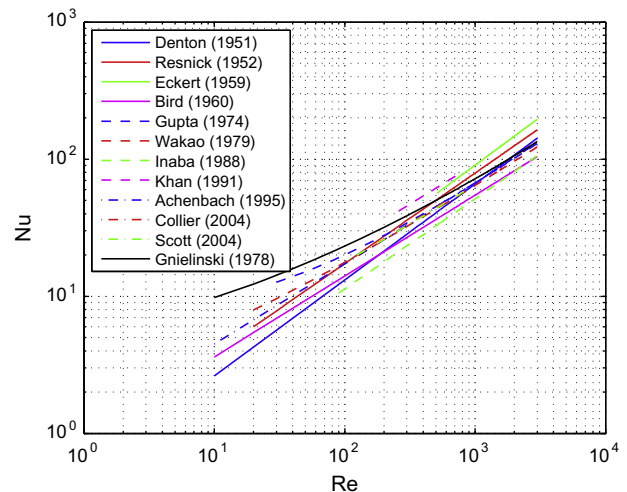

Fig. 2. Nusselt number as a function of Reynolds number for packed beds, data from [31–41] and Eq. (15), i.e. Gnielinski [30].

3.4.2. Radiation

Each particle in the packed bed emits radiation, which is absorbed by neighbouring particles. The influence of the neighbouring particles on radiative heat transfer is considered by changing the boundary condition on the particle surface:

$$q_{rad,i} = \sum_{j=1}^{NP} \epsilon \sigma F_{ij} \left(T_j^4 - T_i^4 \right) \tag{17}$$

where $q_{rad,i}$ is the radiation heat flux from the neighbouring particles to the particle i. ϵ, σ, N and T are the particle emissivity, the Stefan–Boltzmann constant, the number of particles and the particle surface temperature, respectively. F_{ij} is the view factor between particle i and j.

It is difficult, however, to implement Eq. (17) in a simulation, as it requires a summation over all particles for each particle and the calculation of the view factor for each pair of particles. Therefore, an appropriate spherical control volume ϑ is defined around each target particle, see Fig. 3. It is assumed that the target particle exchanges radiation with its surrounding control volume:

$$q_{rad,i} = \epsilon \sigma F_{i\vartheta} \left(T_{\vartheta,i}^4 - T_i^4 \right) \tag{18}$$

Since the target particle is enclosed by the radiation control volume, $F_{i\vartheta} = 1$. The parameter $T_{\vartheta,i}$ is the average temperature of particles and gas phase in the radiation control volume ϑ given by [42]:

$$T_{\vartheta,i} = \phi T_{g,\vartheta} + (1 - \phi) \frac{1}{NP_\vartheta} \sum_{j=1; \neq i}^{NP_\vartheta} T_j \tag{19}$$

where $\phi, T_{g,\vartheta}$ and NP_ϑ are, respectively, the bed porosity, the gas temperature, and the number of particles located in the volume ϑ.

If the target particle is close to a wall, some CFD cells in the radiation control volume are adjacent to the wall. Including the effect of walls on the radiation to the target particle, $T_{\vartheta,i}$ turns out as:

$$T_{\vartheta,i} = (1 - \xi) \left[\phi T_{g,\vartheta} + (1 - \phi) \frac{1}{NP_\vartheta} \sum_{j=1; \neq i}^{NP_\vartheta} T_j \right] + \xi \frac{1}{NC_\vartheta} \sum_{j=1}^{NC_\vartheta} T_{wall,j} \tag{20}$$

where NC_ϑ and T_{wall} are the number of cells in the radiation control volume adjacent to the wall and the wall temperature, respectively. The parameter ξ is a constant which adds weight of the wall temperatures to $T_{\vartheta,i}$. In this study ξ is assumed to be 0.5 to achieve a plausible horizontal temperature profile in the packed bed near the walls.

Thermal radiation from the freeboard above the packed bed is one of the most important mechanisms of grate firing systems. It is responsible for the initiation of the thermo-chemical processes.
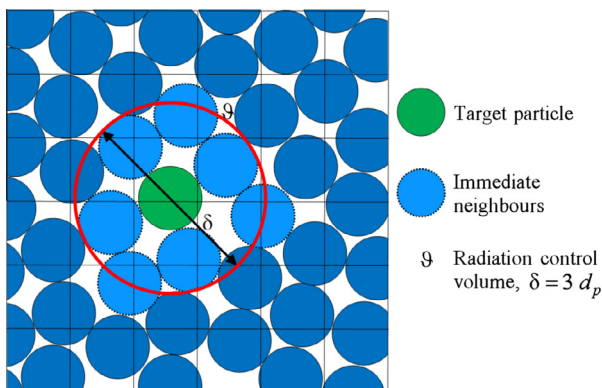
The average radiation temperature for the particles located at the top of the packed bed is calculated by:

$$T_{\vartheta,i} = 0.5 \left(\frac{q_{rad}}{\sigma} \right)^{1/4} + 0.5 \left[\phi T_{g,\vartheta} + (1 - \phi) \frac{1}{NP_\vartheta} \sum_{j=1; \neq i}^{NP_\vartheta} T_j \right] \tag{21}$$

where q_{rad} is the radiation heat flux from the freeboard. It is calculated by the simulation of the gas phase combustion with ANSYS FLUENT [27].

3.5. Gas phase model

Accurate modelling of the system chemistry is critical. In previous studies, mostly global reactions were considered. The global reactions describe an overall process by which reactants are converted to anticipated products at the end of the process. Therefore, they may not be sufficiently accurate for a broad range of operating conditions. The accurate description of the reaction kinetics is of high relevance, since they have a considerable impact on the simulation results. Therefore, in this study detailed mechanisms are used for the homogeneous reactions. A well-known comprehensive reduced mechanism, DRM22, is utilised in this study [43]. It is a 22 species reaction set with 104 elementary reactions reduced from GRI-Mech [44]. The full detailed GRI mechanism version 2.11 [45] has also been applied to evaluate the difference between the full mechanism and the reduced one. It consists of 49 species and 277 reversible reactions. Additionally, the C–H–O subset of the skeletal Kilpinen97 mechanism [46,47], has been applied in order to evaluate the results and applicability of this mechanism for the simulation of biomass grate furnaces. It is a mechanism with 12 species and 25 reactions.

Many different gas species are released during biomass pyrolysis. Several studies investigated the composition of the product gaseous. Most commonly detected gas species are CO, CO_2, H_2, H_2O, CH_4, C_xH_y, CH_mO_n and other trace compounds. In order to use detailed reaction mechanisms, the released gas species in the pyrolysis model must be compatible with the species considered in the mechanisms. Therefore, the products of the pyrolysis reaction in simulations with GRI2.11, DRM22 and Kilpinen97 mechanisms are the intersection of the available species in each mechanism and the most reported gas components in literature. The pyrolysis product compositions considered in simulations with each mechanism are listed in Table 3. Later it is explained how the compositions are calculated. Since there is no C_xH_y and CH_mO_n in the Kilpinen97 mechanism, it was not possible to consider them as pyrolysis products in the simulations with this mechanism.

It is worth noting that the formed tars in the primary pyrolysis reaction are assumed to be fully converted into its main secondary products, e.g. CO, CH_4 and C_2 hydrocarbons. This is due to the fact that the tar composition and chemical formula as well as the rate

Fig. 3. Radiation control volume and neighbouring particles in the packed bed radiation model.

Table 3
The composition of volatiles used in the simulations with different kinetic mechanisms.

Species	Mass fraction		
	GRI2.11	DRM22	Kilpinen97
CO	0.391	0.391	0.492
CO_2	0.170	0.170	0.214
CH_4	0.087	0.087	0.135
H_2	0.017	0.017	0.028
H_2O	0.168	0.168	0.131
N_2	0.001	0.001	0.001
C_2H_2	0.002	0.002	–
C_2H_4	0.002	0.002	–
C_2H_6	0.056	0.056	–
CH_2O	0.107	0.107	–

of its secondary conversion are unknown. This assumption is in line with the dedicated experiments [48,49], in which it was observed that the carbon monoxide is quantitatively the most important product from the homogeneous tar conversion. Over two-thirds of the tar lost at high temperatures forms carbon monoxide. Corresponding methane and C_2 hydrocarbons each account for about 10 wt% of the tar converted. This assumption is plausible for large particles in packed bed condition, because it is known that tar is very reactive when it is in contact with a hot char layer and it easily breaks down.

Conservation equations for C, H, O and N as well as enthalpy provide five equations in order to determine the composition of pyrolysis products. Since the number of equations are less than unknowns, i.e. 10 and 6 unknowns for DRM22 (GRI2.11) and Kilpinen97 mechanisms respectively, the system can have an infinite number of solutions. In order to obtain a meaningful result, some additional constraints are needed. They can be derived form measurements. The experimental data from literature [48–68] are used to calculate the mass ratios of CO, CH_4, H_2 and H_2O to CO_2 and C_2 hydrocarbons to CH_4. They are illustrated in Figs. 4 and 5. The collected data are a compilation of measured values using various fuels, reactors and operating conditions (heating rates, particle sizes, etc.). According to Figs. 4 and 5, the constraints needed can be gained. They are listed in Table 4.

The flow regime in the lab-reactor experiment is laminar ($Re < 2300$). Therefore no turbulence model is required. It highlights the importance of the chemistry model, because the reaction rates are determined by the kinetic mechanism. The radiation which is an important part in combustion simulations is calculated by the Discrete Ordinate Model (DOM) together with the Weighted Sum of Gray Gases (WSGG) method to calculate the radiative absorption and emission coefficients. Mass diffusion coefficients are required whenever species transport equations in multi-component flows are solved. For reacting flows with low turbulence conditions the influence of molecular diffusion on mixing becomes comparable to the contribution of the turbulent diffusion. Hence, the molecular diffusion of each gas species in the mixture was calculated by the kinetic theory [35] instead of using a constant value.
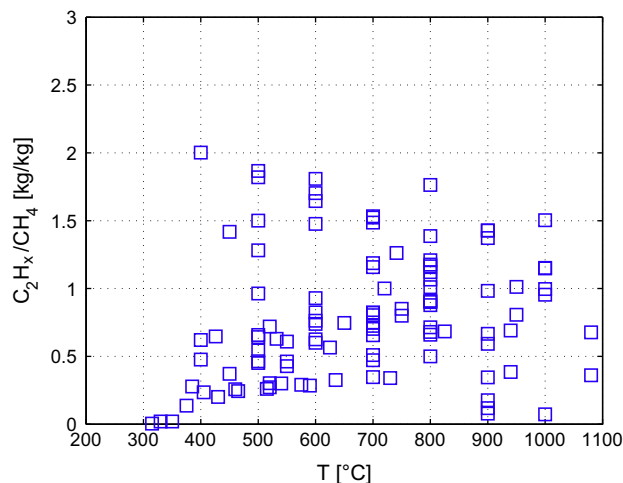

Fig. 5. The mass yield of C_2 hydrocarbons ($C_2H_2 + C_2H_4 + C_2H_6$) in relation to the mass yield of CH_4 as a function of pyrolysis temperature, data from [48–68].

3.6. Boundary conditions

The simulation domain consists of the cylindrical sample holder, the grate, the cylindrical retort, the air inlet tube and the exhaust tube. Scheme of the simulation domain is shown in Fig. 6. Since the outer walls are well insulated, the adiabatic boundary condition is used, except for the walls where the heating elements are located. The heating elements are surrounded by insulation material and controlled separately by two PID controllers to keep their assigned temperatures, i.e. 750 °C for the upper part and 450 °C for the lower part. For the heated wall sections, a temperature dependent boundary condition is needed. If the wall temperature in each section is lower than the assigned temperature, the radiation boundary condition is applied. Once the temperature of the retort wall is higher than the temperatures of the heating elements, there is no heat flux from the heating elements to the retort wall and the insulation avoids any heat loss from
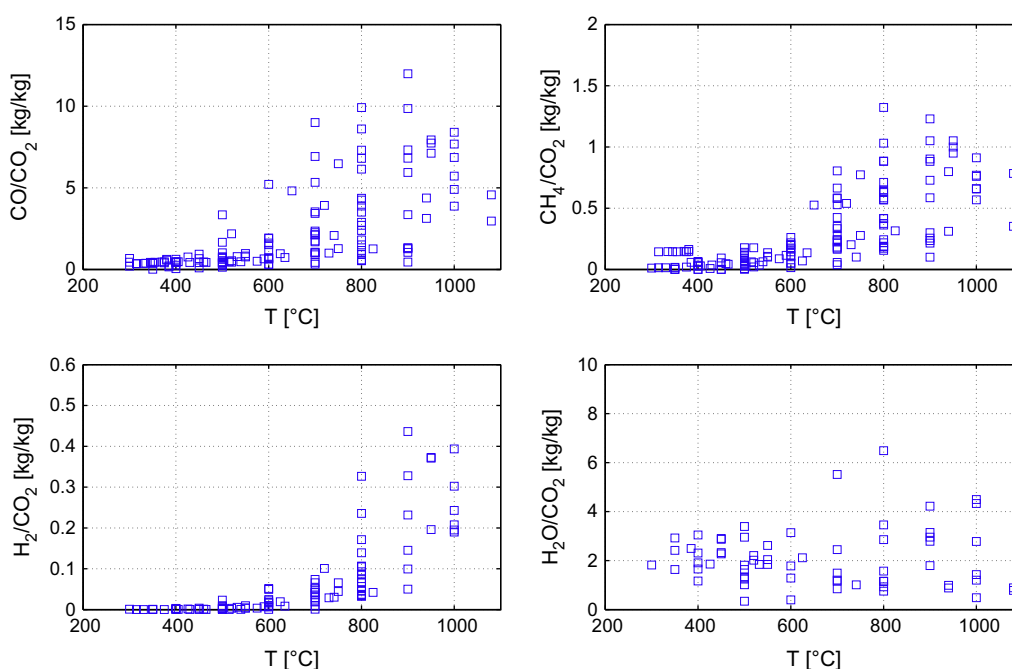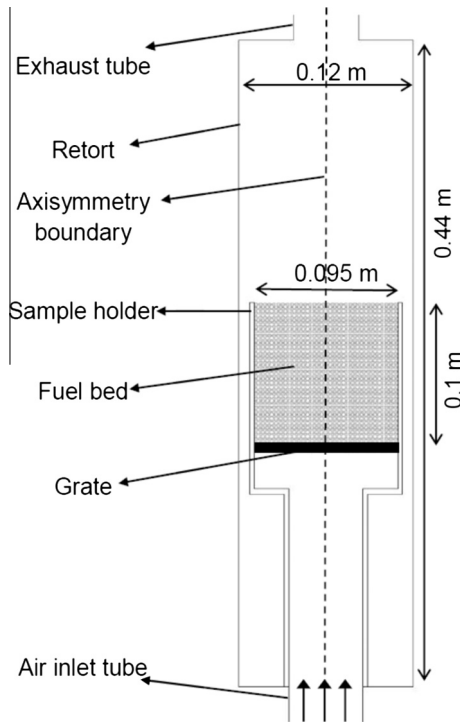

Fig. 4. The mass yields of CO, CH_4, H_2 and H_2O in relation to the mass yield of CO_2 as a function of pyrolysis temperature, data from [48–68].

Table 4
The empirical constraints for the mass yield of volatiles based on Figs. 4 and 5.

$$0.1 < \frac{m_{CO}}{m_{CO_2}} < 10$$

$$0.1 < \frac{m_{CH_4}}{m_{CO_2}} < 1$$

$$0.05 < \frac{m_{H_2}}{m_{CO_2}} < 0.4$$

$$0.5 < \frac{m_{H_2O}}{m_{CO_2}} < 4$$

$$0.1 < \frac{m_{C_2H_2} + m_{C_2H_4} + m_{C_2H_6}}{m_{CO_2}} < .15$$

Fig. 6. Scheme of the simulation domain.

the retort wall. Therefore, the adiabatic boundary condition is applied.

At the beginning of the simulations all particles in the fuel bed have the same size. This is an acceptable assumption, since they are pellets. In each cell of the fuel bed only one parcel (it may be different from a particle, see [27]) is assigned. However, during a simulation it can happen that more than one parcel appears in a cell, due to shrinkage. Since 2D axisymmetric condition has been applied for the simulation, each cell has a different volume depending on its distance from the axis. Therefore, to have an uniform bulk density at the beginning of the simulation in the fuel bed, the mass of each parcel should also be dependent on its distance from the axis. The parcels which are closer to the axis should have less mass than those which are far from the axis. The ratio between the parcel mass and the particle mass is called "particle number per parcel" in Fluent [27] and it determines that each parcel represents how many particles.

3.7. Solution strategy

The pressure based segregated algorithm of ANSYS FLUENT is used as the basis for the computation of the continuous phase and it has been combined with the models describing the conversion of the packed bed. In each flow time step, the fluid properties are updated, then the conservation equations are solved to update

the mass fluxes, pressure and velocities. Afterwards, species and energy equations are solved. These steps are repeated in each flow time step until a converged state is achieved. The converged state of the gas phase serves as boundary condition for the particle model. Discretisation of the differential equations of the flow field is performed in time with the first-order implicit scheme and in space with the second-order upwind scheme. The conservation equations are listed in Table 5.

In the particle model, an adaptive particle time step is used which is mostly smaller than the flow time step. In each particle time step, the boundary temperature, time derivatives of the particle layer temperatures and mass flow rates from each layer are calculated. The Runge–Kutta scheme is used to solve the system of equations. If the relative changes of mass and temperature of each layer are within a tolerance level of 10^{-3}, the particle time step is acceptable, otherwise it is reduced. When the acceptable particle time step is achieved, the mass and temperatures of each layer as well as the particle size and the reaction rates are calculated and the particle state is advanced in time. This procedure is repeated until the flow time is reached. Thereafter, the particle energy and species source terms are returned to the flow solver. A more detailed overview of the particle model solution method is available in [17].

In the packed bed level, once the particles and flow have the same time, the local porosity of each cell inside the bed as well as the bed shrinkage are calculated. Additionally, the radiation temperature and the convective heat transfer coefficient for each particle in the packed bed are calculated before executing the particle subroutine. An overview of the solution algorithm is shown in Fig. 7.

Structure mesh was used for the simulation. To achieve grid independent solutions, several meshes of varying resolution have been tested. It occurred once the cell size was reduced to 3 mm. Additionally, the mesh is refined in the freeboard to 1 mm where mainly the homogeneous reactions happen.

4. Results and discussion

Comparisons between the measured and predicted temperatures in the fuel bed are illustrated in Fig. 8. The positions of thermocouples in the fuel bed are according to Fig. 1. Axisymmetry conditions have been applied to simulate the experimental setup, thus P2a and P2c are corresponding to one point in the simulation domain. In Fig. 9 measured and predicted molar concentrations of O_2, CO, CO_2, CH_4, H_2O and H_2 above the fuel bed (11 cm) are presented. In this section, the results with DRM22 are compared to the experimental data and later the effect of different reaction mechanisms is discussed.

In both experimental and simulation results ignition of volatiles can be recognized, indicated by an abrupt decrease of O_2

Table 5
Conservation equations.

$$\frac{\partial}{\partial t}(\phi \rho_g) + \nabla \cdot (\phi \rho_g \vec{u}) = S_{con}$$

$$\frac{\partial}{\partial t}(\phi \rho_g \vec{u}) + \nabla \cdot (\phi \rho_g \vec{u}\vec{u}) = -\phi \nabla p + \nabla \cdot \tilde{\tau} + \phi \rho_g \vec{g} + \vec{S}_m$$

$$\frac{\partial}{\partial t}(\phi \rho_g c_{p,g} T_g) + \nabla \cdot (\phi \rho_g \vec{u} c_{p,g} T_g) = \nabla \cdot (\phi \lambda_{g,e} \nabla T_g) + S_q$$

$$\frac{\partial}{\partial t}(\phi \rho_g \omega_i) + \nabla \cdot (\phi \rho_g \vec{u} \omega_i) = \nabla \cdot (\phi \rho_g \mathcal{D} \nabla \omega_i) + S_{s,i}$$

$$S_{con} = \psi v_{H_2O} r_{dry} + \psi \sum_k v_k r_{pyr} + \psi \sum_n \sum_m v_m r_{ch,n}$$

k: pyrolysis products; n: char burnout reactions;
m: species involved in char burnout reactions see Table 2

$$\vec{S}_m = -\left(\frac{\mu}{C_1}\vec{u} + C_2 \rho_g |u|\vec{u}\right)$$

$$S_q = \psi h S_p (T_p - T_g) + \psi \sum_j c_{p,j} \dot{m}_j (T_p - T_g)$$
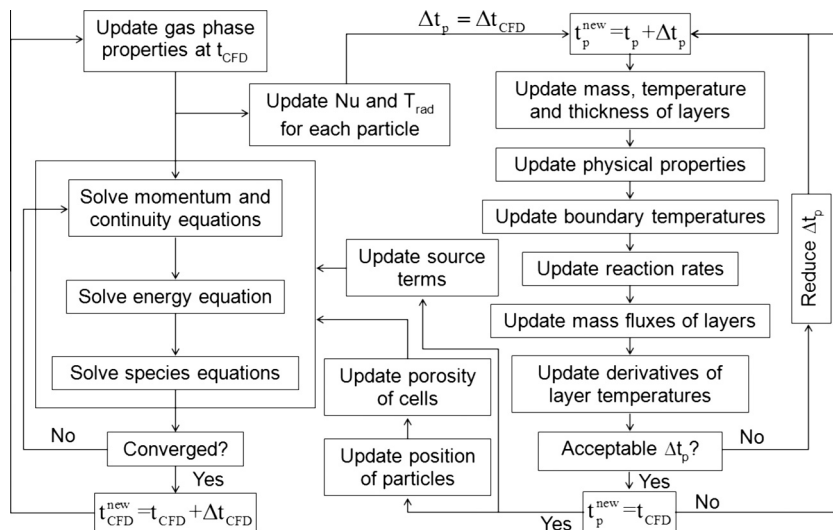
$$S_{s,i} = \psi \sum_l v_l r_l$$
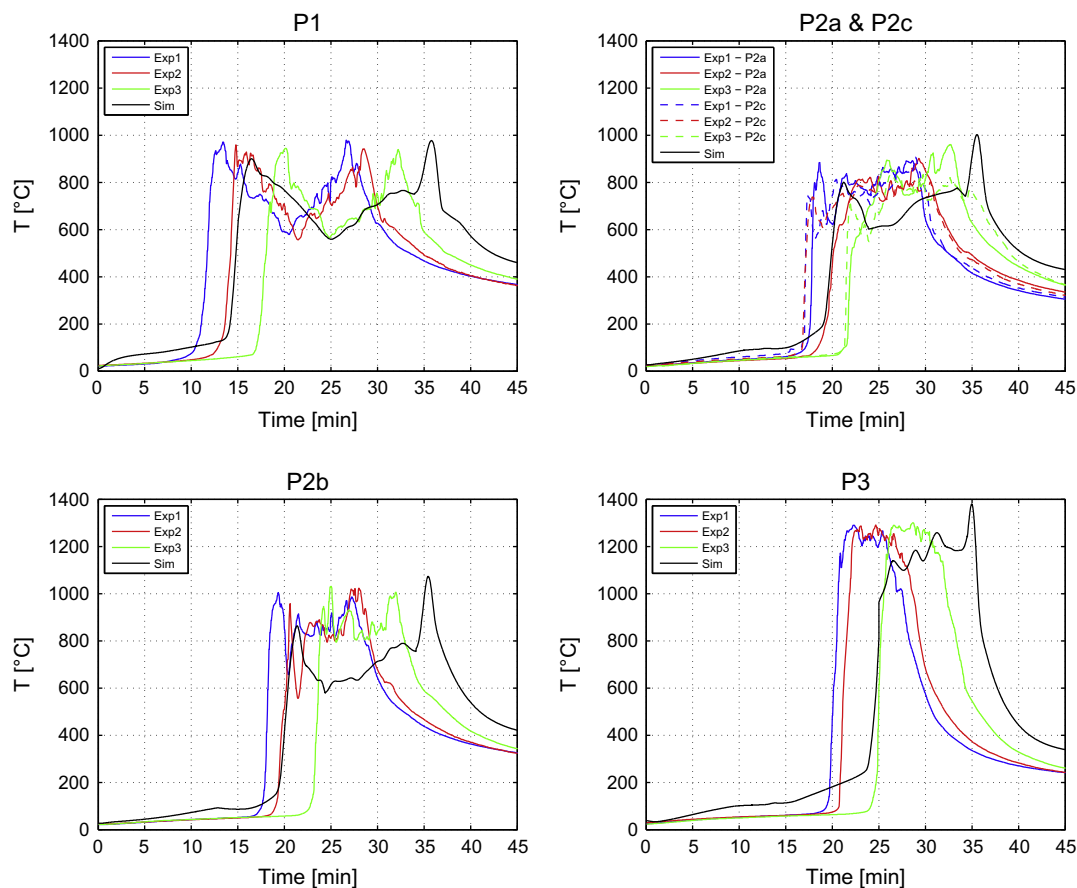
Fig. 7. Overview of the solution algorithm.

Fig. 8. Comparison between simulated and measured temperatures at different positions inside the packed bed.

concentrations and sharp increases of CO, CO_2, H_2O and H_2 concentrations. Afterwards, the thermal conversion of the packed bed accelerates. After the ignition, the simulated species concentrations depict similar trends as the measured values, except H_2O. In the simulation, in contrast to the experimental data, H_2O declines. The main reason for the sharp increase of H_2O, once the ignition occurs, is combustion in the gas phase. When oxygen depletes, H_2O mole fraction reduces to 0.1. Afterwards, it follows the trend of the experiments, however, with lower concentration.

The reason of this deviation can be a lower concentration of water vapour in the composition of volatiles than the experiments. It is worth noting that in this study the composition of volatiles is determined by mass and energy balances. Most probably a mechanistic pyrolysis scheme, where the composition of volatiles is temperature dependent, could improve the results concerning H_2O.

The volatiles combustion front propagates downwards in the packed bed. Once the combustion front reaches a thermocouple, the temperature sharply increases. The steep increase in

temperature occurs first at P1 then at P2 and finally at P3. The measured temperatures at P2a and P2c rise almost simultaneously, except the second test run (Exp2). The temperature rise at P2b occurs slightly after P2a and P2c. The model predicts well the first peak temperatures and their sequences. The temperature at each point inside the packed bed decreases after the combustion front has passed by. However, it remains relatively high, because the hot flue gas passes through the bed. The simulation results at P1, P2a and P2c comply with the experimental data concerning the gradual decline of temperatures. The model predicts lower temperatures at P2b after the first temperature peak in comparison to the measured values. In addition, the steep increase in temperature at P3 is slightly delayed in comparison to the measured values. It implies that in the simulation the heat diffusion in the packed bed and the conversion rate is slower than in the experiments. This might be attributed to the heat transfer model inside the packed bed and also uncertainties of the physical properties, i.e. thermal conductivity.

Measured and modelled O_2 concentrations above the fuel bed show that the entire oxygen is consumed by the combustion of pyrolysis products during the devolatilisation step. Therefore, the biomass char remains mostly unreacted behind the combustion front. As the combustion front reaches the grate, after about 25 min in the simulation, the temperature at P3 abruptly rises and concentrations of H_2O, H_2 and CH_4 sharply decline which indicates the end of the pyrolysis process. At the end of pyrolysis, both model and experimental data show the same behaviour, except CO and CO_2 concentrations which deviate from the experimental data. In the model CO decreases, while the first and the second test runs (Exp1 and Exp2) show a gradual increase and the third one (Exp3) a slight decrease. The predicted CO_2 concentrations rise while the experiments depict a decrease of CO_2 at the end of pyrolysis and beginning of char burnout.

Sharp decrease of CO_2 in the experiments at the beginning of char burnout can be attributed to the fact that CO_2 produced by the char oxidation reaction is consumed by gasification reactions.
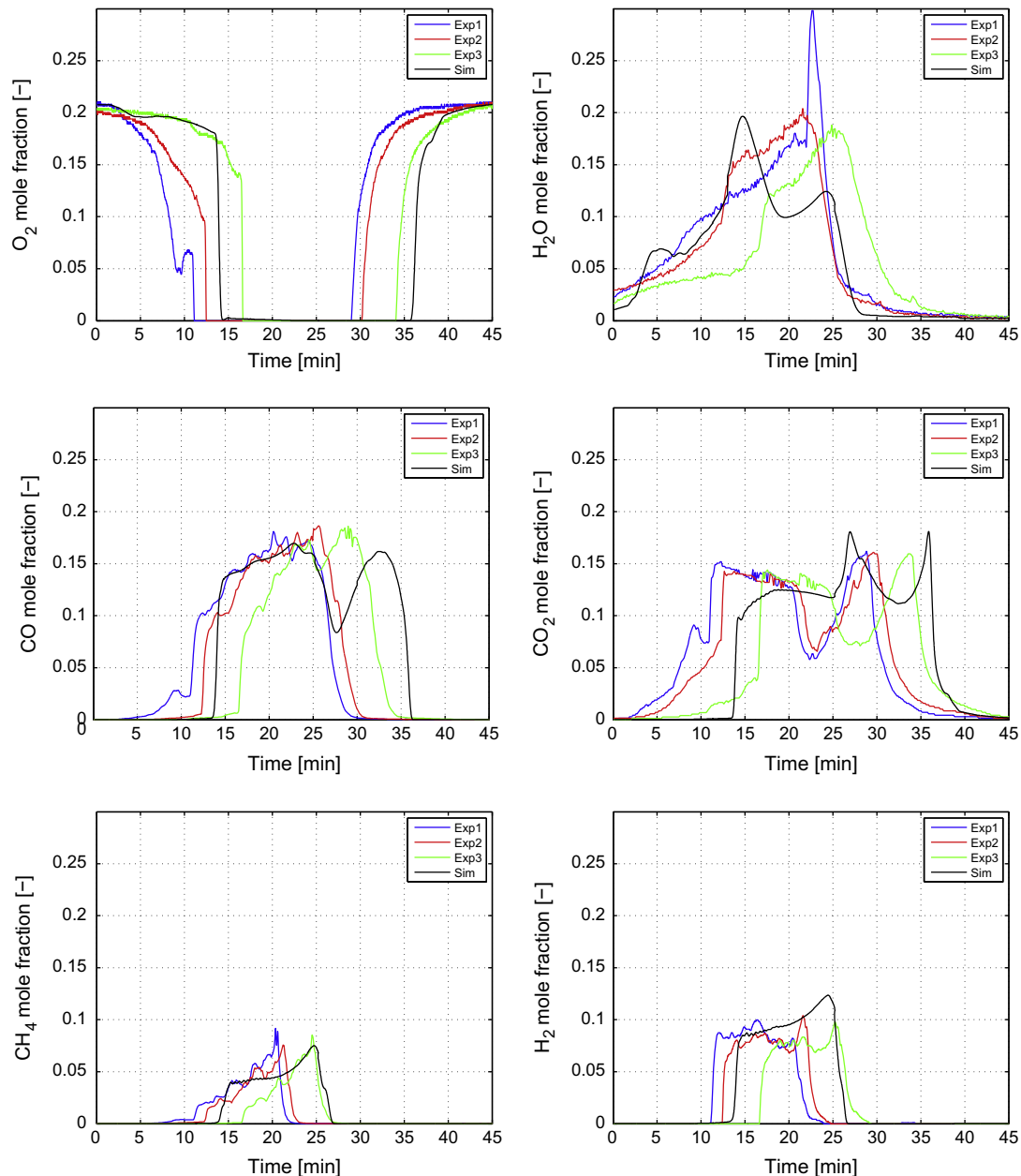

Fig. 9. Comparison between simulated and measured species concentrations at a height of 11 cm above the initial surface of the packed bed.
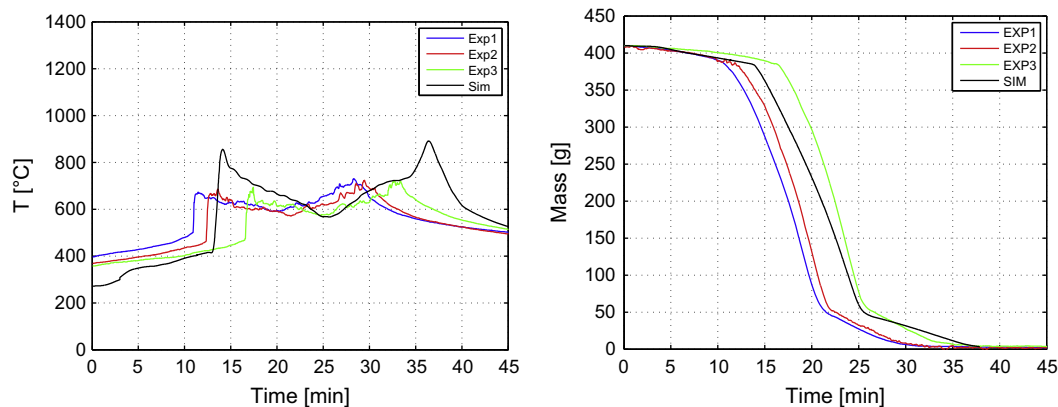
Fig. 10. Left: Comparison between simulated and measured flue gas temperatures in the freeboard at a height of 7.5 cm above the initial surface of the packed bed and 4 cm away from the retort wall; Right: Comparison between simulated and measured mass loss profiles.

However, there are some reasons for increase of CO_2 and decrease of CO in the simulation at the beginning of char burnout. First, the correlations for the CO to CO_2 product ratio for the char oxidation reaction predict more CO_2 than CO at low temperatures, i.e. beginning of char oxidation. Second, at the beginning of char burnout the temperatures predicted at P2 and P3 are lower than the measured values. This leads to a lower gasification reaction rate in the simulation. Lastly, it may also be attributed to an over-prediction of the CO conversion by the water–gas shift reaction in the simulation because of lower temperatures in the simulation at the beginning of char burnout. By increasing temperature in the simulation more CO than CO_2 is produced by the char oxidation reaction and the rate of gasification reactions increases. Hence, in the simulation CO_2 starts to decrease and CO rises, as it can be seen in Fig. 9.

Char burnout happens close to the grate, since the air is introduced from below. During char oxidation, the oxygen is consumed near the grate. Once char oxidation starts, the bed temperatures at P1 and P2 start to gradually rise. It attributes to the heat generated by char combustion. Approaching the end of char burnout, the air to fuel ratio increases which promotes the homogeneous CO oxidation reaction. It results in sharp peaks in the CO_2 concentrations and temperatures at all thermocouple locations, particularly at P1 and P2, in both simulation and experimental data.

To evaluate the predicted propagation rate of the reaction front, the time difference between the first temperature peaks at P1, P2b and P3 have to be compared with the measured values. This comparison shows that the model predicts a slower propagation rate, 0.08 (kg m^{-2} s^{-1}), while the propagation rate according to the
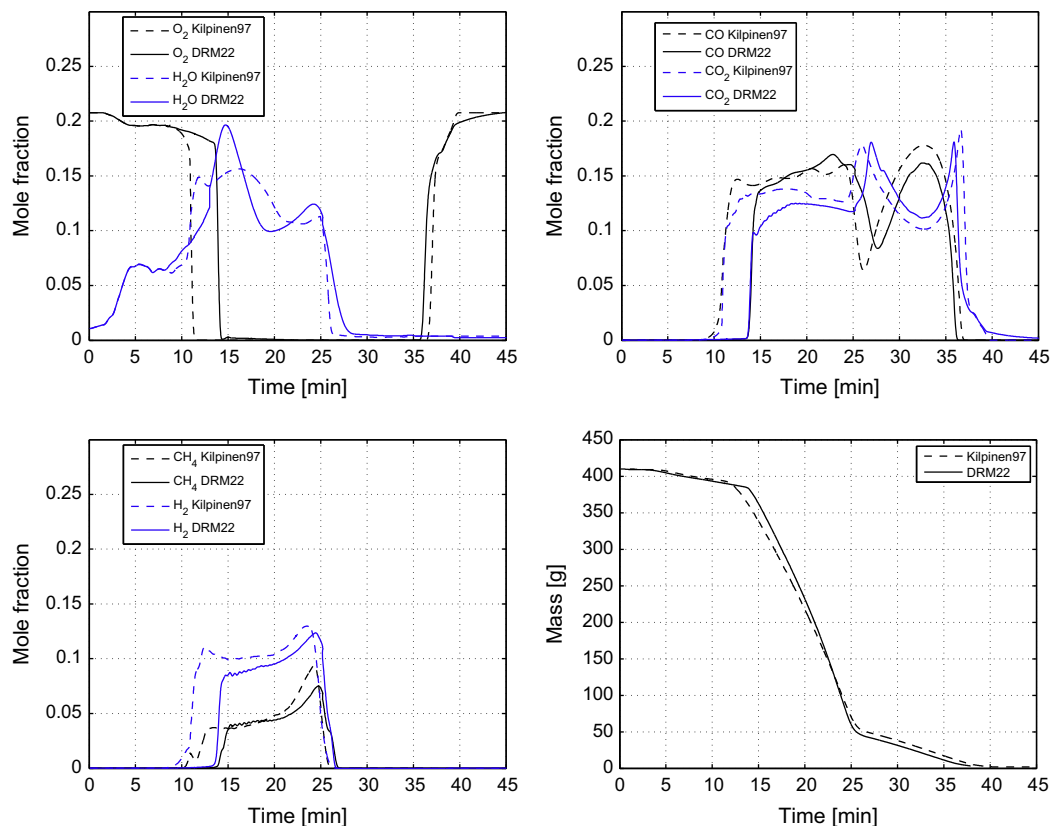

Fig. 11. Comparison between the results of the DRM22 and Kilpinen97 mechanisms for species concentrations in the freeboard and mass loss profiles.

experiments ranges from 0.09 to 0.12 (kg m^{-2} s^{-1}). The calculated propagation rate is comparable with the measured values of Porteiro et al. [3] for the combustion of wood pellets in a fixed bed reactor.

Some previous works reported a secondary reaction front, i.e. the char burnout front, propagating upwards towards the top of the packed bed and burning the char previously formed. This is true when the bed does not collapse and it retains its original structure. However, if biomass has a low ash content which forms a thin ash layer on a grate, it is more plausible that the char burnout front stays close to the grate and the biomass char particles on the grate are replaced by the upper particles when they are completely burned. The simulation results confirm this hypothesis. According to the simulations, char burnout happens on the grate in a region with a height of about 2–3 times of the initial particle size and above this region O_2 concentrations are zero, almost for the entire char oxidation process.

Moreover, the predicted flue gas temperature has been compared with the experimental data in Fig. 10. The thermocouples are located 7.5 cm above the initial surface of the packed bed and 4 cm away from the wall of the retort, see Fig. 1. Both thermocouples measured rather similar temperature profiles. Since the reactor geometry has been modelled axisymmetrically, the predicted flue gas temperatures at these positions have been compared to the average values of the two thermocouple temperatures in each test run. Both measured and simulation results show the same trends concerning the flue gas temperature. The first temperature peak corresponds to the ignition of the pyrolysis products and the second peak is related to the end of char burnout where the air to fuel ratio increases. The deviation in the temperature peaks between experiments and simulations might be due to the limitations of measuring flue gas temperature with thermocouples (the colder retort wall affects the thermocouple measurements by radiation).

The mass loss profile of the fuel bed over time is also shown in Fig. 10. Three different periods can be distinguished based on the mass loss curves. The first one is the drying period in combination with pyrolysis without ignition of volatiles. Once ignition of volatiles happens most of the volatiles are released and the mass of the packed bed sharply declines with almost constant rate. After the end of the pyrolysis period, the remaining mass in the reactor is the same for all experiments and simulation results, about 50 g. During the char oxidation period the mass of the packed bed gradually decreases, as the char burnout rate is slower than the pyrolysis rate. According to the experiments the final remaining mass after char burnout is between 0.9 and 1.4 (g), the model prediction is 1.1 (g).

Both experimental and simulation results depict the same combustion behaviour in the packed bed. The predicted trends of the species concentrations and the temperature profiles are similar to the experimental data. However, there are deviations from the experiments regarding H_2O concentrations right after the ignition of volatiles and CO and CO_2 concentrations at the end of pyrolysis and the beginning of char burnout. The positions and the amounts of the peaks concerning the species concentrations as well as temperatures are well predicted, except for the maximum flue gas temperature. The conversion of the packed bed in the model lasts slightly longer than in the experiments. Some further developments may eliminate the current drawbacks of the model, such as improvements of the packed bed heat transfer model as well as a more enhanced pyrolysis scheme (e.g. a mechanistic scheme).

4.1. Effect of the gas phase reaction mechanism

In order to investigate the influence of the mechanism applied for modelling the reaction chemistry the results of the full mechanism (GRI2.11), the reduced mechanism (DRM22) and the skeletal mechanism (Kilpinen97) have been compared. There is hardly any difference between the results of GRI2.11 and DRM22. Therefore, in Figs. 11 and 12, only the results of DRM22 and Kilpinen97 are compared.

As it has already been mentioned, the Kilpinen97 mechanism includes no C_xH_y and CH_mO_n species. Hence, the composition of volatiles in the simulation with this mechanism consists of a lower number of species in comparison to DRM22 and they cannot have similar composition. Therefore, in the calculations of the volatiles composition for Kilpinen97 the mass ratios of CO/CO_2, CH_4/CO_2 and H_2/CO_2 are considered to be as similar as possible to the corresponding ratios in the simulation with DRM22. In this way, the input parameters of the simulations with DRM22 and Kilpinen97 are better comparable. The comparison depicts that the skeletal mechanism Kilpinen97 with a considerably lower number of reactions and species than GRI2.11 and DRM22 can predict the species and temperature profiles as well as the mass loss evolution with acceptable accuracy for engineering applications. It is worth noting that the application of Kilpinen97 reduces the calculation time by about 17% in comparison to DRM22.

4.2. Bed shrinkage and porosity

As an indication of the bed shrinkage, a change of the normalised height of the fuel bed over time is shown in Fig. 13. The surface of the fuel bed is not flat during the conversion of the packed bed because of the uneven consumption of the fuel. Therefore, in
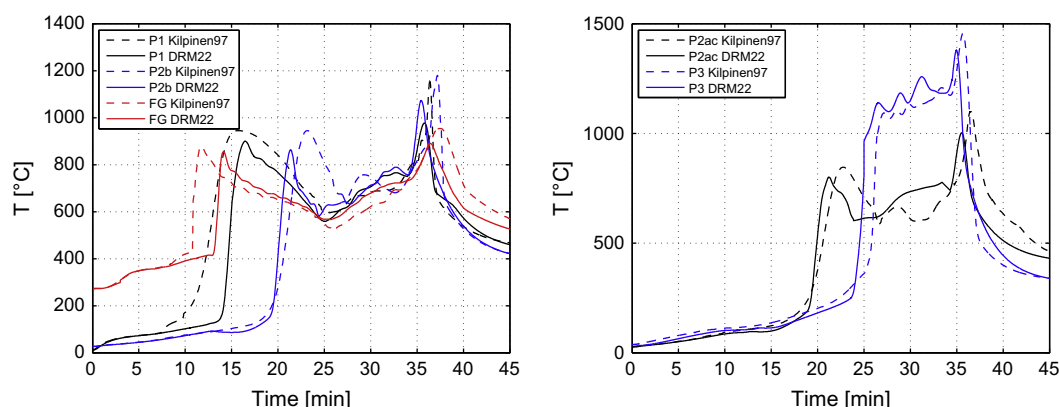

Fig. 12. Comparison between the results of the DRM22 and Kilpinen97 mechanisms for temperatures inside the packed bed (P1, P2b, P2ac, P3) and freeboard (FG).
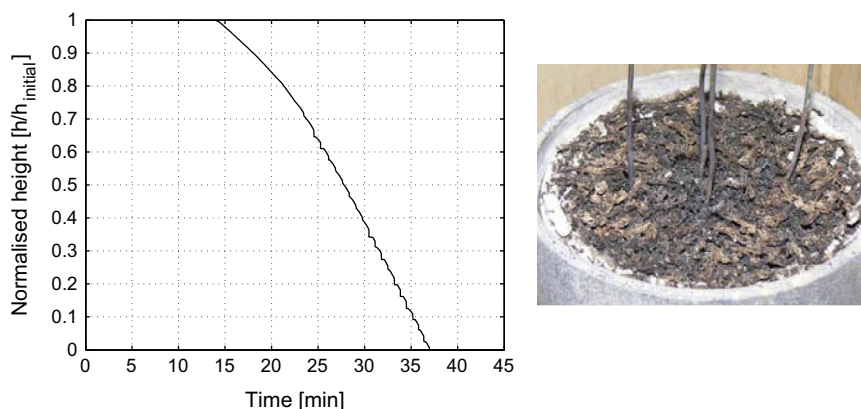
Fig. 13. Left: Normailsed height of the bed; Right: Picture of the remaining ash layer on the grate at the end of a test run.
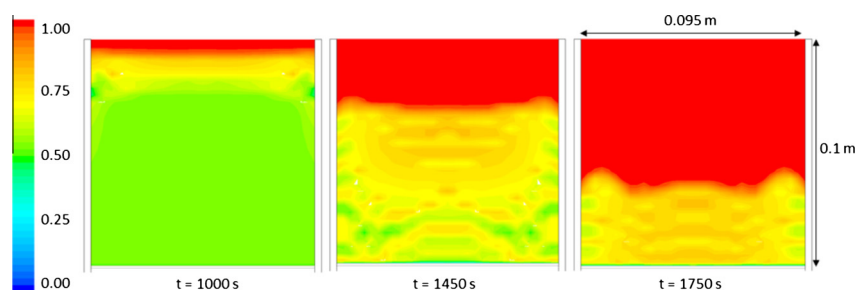

Fig. 14. Porosity contours in the fuel bed at three different times.

Fig. 13 always the highest point of the surface of the bed has been considered. As it can be seen shrinkage starts with pyrolysis, because in the particle model it is postulated that during drying, the size of the particles remains constant, which is a plausible assumption [20]. The height of the fuel bed at the end of pyrolysis amounts to about 61% of the initial height. This is in line with previous findings of Kumar et al. [20], who reported a volume loss variation of 35–55%. As char burnout initiates, the decrease in bed height is not smooth anymore. The discontinuous local shrinkage can be interpreted as a bed collapse. However, by employing specific models for the bed collapse, such as [9], the results may be further improved.

Since the movement of the particles is only considered in gravity direction, it leads to an unrealistic shape of the ash layer on the grate at the end of char burnout. Therefore, it is assumed that as soon as a particle only contains ash and it reaches the grate it will be excluded from the calculation. As a consequence of this assumption the calculated bed height approaches to zero at the end of char burnout, see Fig. 13. This is an acceptable assumption, because the ash content of wood pellets is very low. Moreover, as it can be seen in Fig. 13, in the test runs at the end of char burnout an ash layer with a height of only a few millimetres and mass of about 0.9–1.4 g was remained.

The local porosity inside the fuel bed influences the heat transfer and the flow field in the bed. The local porosity is affected by the bed shrinkage and the uneven consumption of fuel. Fig. 14 shows the calculated local porosity inside the fuel bed. The bed porosity at the beginning is assumed to be constant and equal to 0.55 – a value derived from the bulk and particle density of the fuel used. The initial constant porosity of the bed changes, due to the uneven consumption of fuel particles and bed shrinkage. Due to the shrinkage of the bed, the upper part of the sample holder becomes empty and its porosity turns to one. Moreover, the uneven surface of the fuel bed can be seen in Fig. 14. According to the

simulations, the conversion of the biomass particles in the centre of the sample holder is faster, particularly during char burnout. This can be attributed to the heat transfer to the wall of the sample holder from the particles near the wall which reduces particle temperatures.

5. Summary and conclusions

An unsteady three-dimensional model for the combustion of biomass packed beds is presented. The calculations of the freeboard region and the packed bed are combined. The model is able to capture the smooth shrinkage of the bed as well as the discontinuous shrinkage (bed collapse). The interactions between the gas and solid phases as well as the radiative heat transfer between the particles are considered. The biomass particles in the packed bed are modelled as thermally thick particles. Experimental results were obtained under fuel rich conditions with a laboratory-scale fixed bed reactor in order to validate the model and to obtain a better understanding of the combustion processes. The experimental data include gas species concentrations above the bed, bed temperatures, flue gas temperatures in the freeboard and mass loss evolution.

The packed bed model has been extensively validated concerning the temperature profiles at different heights in the packed bed and above the bed, several species concentrations in the freeboard as well as the propagation of the reaction front in the packed bed. The results of the model are in good agreement with the experimental data.

An accurate model for the combustion chemistry in the freeboard is of importance, due to its strong interactions with the packed bed. Hence, three combustion chemistry mechanisms have been investigated. The GRI2.11 and DRM22 mechanisms gave almost identical results. The predicted flue gas temperature and

species concentrations in the freeboard with the Kilpinen97 mechanism are acceptable. However, considering the fact that the skeletal Kilpinen97 mechanism has a considerably lower number of species and reactions than the two other mechanisms, it can be concluded that for engineering applications where the reduction of calculation time is important, the Kilpinen97 mechanism is preferable to the more detailed mechanisms. Additionally, the mechanisms investigated, especially DRM22 and GRI2.11, predict the ignition time and formation of the flame in the gas phase well.

The presented model covers certain advantages/improvements concerning the avoidance of the separation between packed bed and freeboard modelling, the consideration of biomass particles as thermally thick and the consideration of bed shrinkage. Models already published typically cover only one of these features. The present version of the model with a priori particle trajectories is currently being used to simulate biomass grate furnaces within a feasible calculation time. However, the model has some limitations: the movement of the particles is only considered in gravity direction and the effect of moving grate bars on the packed bed needs to be modelled. These issues need to be addressed in further developments of the model, to improve and extend its applicability to a wider range of biomass grate firing systems.

References

[1] Ryu C, Yang YB, Khor A, Yates NE, Sharifi VN, Swithenbank J. Effect of fuel properties on biomass combustion: Part I. Experiments–fuel type, equivalence ratio and particle size. Fuel 2006;85:1039–46.

[2] van der Lans RP, Pedersen LT, Jensen A, Glarborg P, Dam-Johansen K. Modelling and experiments of straw combustion in a grate furnace. Biomass Bioenergy 2000;19:199–208.

[3] Porteiro J, Patino D, Collazo J, Granada E, Moran J, Miguez JL. Experimental analysis of the ignition front propagation of several biomass fuels in a fixed-bed combustor. Fuel 2010;89:26–35.

[4] Porteiro J, Patino D, Miguez JL, Granada E, Moran J, Collazo J. Study of the reaction front thickness in a counter-current fixed-bed combustor of a pelletised biomass. Combus Flame 2012;159:1296–302.

[5] Merrick D. Mathematical models of the thermal decomposition of coal. 1. The evolution of volatile matter. Fuel 1983;62:534–9.

[6] Shin D, Choi S. The combustion of simulated waste particles in a fixed bed. Combust Flame 2000;121:167–80.

[7] Di Blasi C. Dynamic behaviour of stratified downdraft gasifiers. Chem Eng Sci 2000;55:2931–44.

[8] Saastamoinen JJ, Taipale R, Horttanainen M, Sarkomaa P. Propagation of the ignition front in beds of wood particles. Combust Flame 2000;123:214–26.

[9] Hermansson S, Thunman H. CFD modelling of bed shrinkage and channelling in fixed-bed combustion. Combust Flame 2011;158:988–99.

[10] Yang YB, Goh YR, Zakaria R, Nasserzadeh V, Swithenbank J. Mathematical modelling of MSW incineration on a travelling bed. Waste Manage 2002;22:369–80.

[11] Collazo J, Porteiro J, Patino D, Granada E. Numerical modeling of the combustion of densified wood under fixed-bed conditions. Fuel 2012;93:149–59.

[12] Duffy NT, Eaton JA. Investigation of factors affecting channelling in fixed-bed solid fuel combustion using CFD. Combust Flame 2013;106:2204–20.

[13] Peters B. Measurements and application of a discrete particle model (DPM) to simulate combustion of a packed bed of individual fuel particles. Combust Flame 2002;131:132–46.

[14] Mehrabian R, Stangl S, Scharler R, Obernberger I, Weissinger A. CFD simulation of biomass grate furnaces with a comprehensive 3D packed bed model. In: Proc of 25th German flame day, Karlsruhe, Germany; 2011.

[15] Simsek E, Brosch B, Wirtz S, Scherer V, Krüll F. Numerical simulation of grate firing systems using a coupled CFD/discrete element method (DEM). Powder Technol 2009;193:266–73.

[16] Anca-Couce A, Zobel N, Jakobsen HA. Multi-scale modeling of fixed-bed thermo-chemical processes of biomass with the representative particle model: application to pyrolysis. Fuel 2013;103:773–82.

[17] Mehrabian R, Zahirovic S, Scharler R, Obernberger I, Kleditzsch S, Wirtz S, et al. A CFD model for thermal conversion of thermally thick biomass particles. Fuel Process Technol 2012;95:96–108.

[18] Stubenberger G, Scharler R, Zahirovic S, Obernberger I. Experimental investigation of nitrogen species release from different solid biomass fuels as a basis for release models. Fuel 2008;87:793–806.

[19] Thunman H, Leckner B, Niklasson F, Johnsson F. Combustion of wood particles a particle model for Eulerian calculations. Combust Flame 2002;129:30–46.

[20] Kumar RR, Kolar AK, Leckner B. Shrinkage characteristics of Casuarina wood during devolatilization in a fluidized bed combustor. Biomass Bioenergy 2006;30:153–65.

[21] Bergström D, Israelsson S, Öhman M, Dahlqvist S, Gref R, Boman C, et al. Effects of raw material particle size distribution on the characteristics of Scots pine sawdust fuel pellets. Fuel Process Technol 2008;89:1324–9.

[22] Grønli MG. A theoretical and experimental study of the thermal degredation of biomass. PhD thesis, The Norwegian University of Science and Technology; 1996.

[23] Lu H. Experimental and modelling investigation of biomass particle combustion. PhD thesis, Brigham Young University; 2006.

[24] Branca C, Albano A, Di Blasi C. Critical evaluation of wood devolatilization mechanisms. Thermochim Acta 2005;429:133–41.

[25] Sreekanth M, Sudhakar DR, Prasad BVSSS, Kolar AK, Leckner B. Modelling and experimental investigation of devolatilizing wood in a fluidized bed combustor. Fuel 2008;87:2698–712.

[26] Johansson R, Thunman H, Leckner B. Influence of intraparticle gradients in modeling of fixed bed combustion. Combust Flame 2007;149:49–62.

[27] ANSYS Inc., ANSYS Fluent Theory Guide, Release 14.5; 2012.

[28] Idelchik IE. Handbook of hydraulic resistance. 3rd ed. Begell House; 1996.

[29] Botterill JSM, Salway AG, Teoman Y. The effective thermal conductivity of high temperature particulate beds – I. Experimental determination. Int J Heat Mass Transf 1989;32:585–93.

[30] Gnielinski V. Gleichungen zur Berechnung des Wärme- und Stoffaustausches in durchströmten ruhenden Kugelschüttungen bei mittleren und grossen Pecletzahlen. Verfahrenstechnik 1978;12:363–6.

[31] Gupta SN, Chaube RB, Upadhyay SN. Fluid-particle heat transfer in fixed and fluidized beds. Chem Eng Sci 1974;29:839–43.

[32] Denton WH. The heat transfer and flow Resistance for fluid flow through randomly packed spheres. In: The general discussion on heat transfer. London: Institute of Mechanical Engineers and ASME; 1951. p. 370–3.

[33] Resnick H. Simultaneous heat and mass transfer in a diffusion-controlled chemical reaction. PhD thesis, MIT, USA; 2006.

[34] Eckert ERG, Drake RMJ. Heat and mass transfer. New York: McGraw-Hill; 1959.

[35] Bird RB, Stewart WE, Lightfoot EN. Transport phenomena. New York: John Wiley & Sons; 2002.

[36] Wakao N, Kaguei S, Funazkri T. Effect of fluid dispersion coefficients on particle-to-fluid heat transfer coefficients in packed beds: correlation of Nusselt numbers. Chem Eng Sci 1979;34:325–36.

[37] Inaba H, Fukuda T, Saito H, Mayinger F. Transient behavior of heat removal from a cylindrical heat storage vessel packed with spherical porous particles. Wärme- und Stoffübertragung 1988;22:325–33.

[38] Khan JA, Beasley DE, Alatas B. Evaporation from a packed bed of porous particles into superheated vapor. Int J Heat Mass Transf 1991;34:267–80.

[39] Achenbach E. Heat and flow characteristics of packed beds. Exp Thermal Fluid Sci 1995;10:17–27.

[40] Collier AR, Hayhurst AN, Richardson JL, Scott SA. The heat transfer coefficient between a particle and a bed (packed or fluidised) of much larger particles. Chem Eng Sci 2004;59:4613–20.

[41] Scott SA, Davidson JF, Dennis JS, Hayhurst AN. Heat transfer to a single sphere immersed in beds of particles supplied by gas at rates above and below minimum fluidization. Ind Eng Chem Res 2004;43:5632–44.

[42] Zhou ZY, Yu AB, Zulli P. Particle scale study of heat transfer in packed and bubbling fluidized beds. AIChE J 2009;55:868–84.

[43] Kazakov A, Frenklach M. <http://www.me.berkeley.edu/drm/>.

[44] Frenklach M, Wang H, Yu CL, Goldenberg M, Bowman CT, Hanson RK, et al. <http://www.me.berkeley.edu/gri-mech/>.

[45] Bowman CT, Hanson RK, Davidson DF, Gardiner WC, Lissianski V, Smith GP, et al. <http://www.me.berkeley.edu/gri-mech/>.

[46] Kilpinen P. pia.kilpinen@uku.fi or pia.kilpinen@abo.fi.

[47] Zahirovic S, Scharler R, Kilpinen P, Obernberger I. A kinetic study on the potential of a hybrid reaction mechanism for prediction of NOx formation in biomass grate furnaces. Combust Theory Model 2011;15:645–70.

[48] Boroson ML, Howard JB, Longwell JP, Peters WA. Product yields and kinetics from the vapor phase cracking of wood pyrolysis tars. AIChE J 1989;35:120–8.

[49] Graham RG, Bergougnou MA, Overend RP. Fast pyrolysis of biomass. J Anal Appl Pyrol 1984;6:95–135.

[50] Nunn TR, Howard JB, Longwell JP, Peters WA. Product compositions and kinetics in the rapid pyrolysis of sweet gum hardwood. Ind Eng Chem Process Des Dev 1985;24:836–44.

[51] Hajaligol MR, Howard JB, Longwell JP, Peters WA. Product compositions and kinetics for rapid pyrolysis of cellulose. Ind Eng Chem Process Des Dev 1982;21:457–65.

[52] Di Blasi C, Signorelli G, Di Russo C, Rea G. Product distribution from pyrolysis of wood and agricultural residues. Ind Eng Chem Res 1999;38:2216–24.

[53] Di Blasi C, Branca C, Santoro A, Gonzalez HE. Pyrolytic behavior and products of some wood varieties. Combust Flame 2001;124:165–77.

[54] Horne PA, Williams PT. Influence of temperature on the products from the flash pyrolysis of biomass. Fuel 1996;75:1051–9.

[55] Agblevor FA, Besler S, Wiselogel AE. Fast pyrolysis of stored biomass feedstocks. Energy Fuels 1995;9:635–40.

[56] Wang X, Kersten SRA, Prins W, van Swaaij WPM. Biomass pyrolysis in a fluidized bed reactor. Part 2: Experimental validation of model results. Ind Eng Chem Res 2005;44:8786–95.

[57] Fagbemi L, Khezami L, Capart R. Pyrolysis products from different biomasses: application to the thermal cracking of tar. Appl Energy 2001;69:293–306.

[58] Scott DS, Piskorz J, Bergougnou MA, Graham R, Overend RP. The role of temperature in the fast pyrolysis of cellulose and wood. Ind Eng Chem Res 1988;27:8–15.

[59] Becidan M, Skreiberg Ø, Hustad JE. Products distribution and gas release in pyrolysis of thermally thick biomass residues samples. J Anal Appl Pyrol 2007;78:207–13.

[60] de Jong W, Pirone V, Wójtowicz MA. Pyrolysis of Miscanthus Giganteus and wood pellets: TG-FTIR analysis and reaction kinetics. Fuel 2003;82:1139–47.

[61] Dupont C, Commandré JM, Gauthier P, Boissonnet G, Salvador S, Schweich D. Biomass pyrolysis experiments in an analytical entrained flow reactor between 1073 K and 1273 K. Fuel 2008;87:1155–64.

[62] Dupont C, Chen L, Cances J, Commandre JM, Cuoci A, Pierucci S, et al. Biomass pyrolysis: kinetic modelling and experimental validation under high temperature and flash heating rate conditions. J Anal Appl Pyrol 2009;85:260–7.

[63] Beaumont O, Schwob Y. Influence of physical and chemical parameters on wood pyrolysis. Ind Eng Chem Process Des Dev 1984;23:637–41.

[64] Encinar JM, González JF, González J. Fixed-bed pyrolysis of Cynara cardunculus L. product yields and compositions. Fuel Process Technol 2000;68:209–22.

[65] Wei L, Xu S, Zhang L, Zhang H, Liu C, Zhu H, et al. Characteristics of fast pyrolysis of biomass in a free fall reactor. Fuel Process Technol 2006;87:863–71.

[66] Aguado R, Olazar M, San José MJ, Aguirre G, Bilbao J. Pyrolysis of sawdust in a conical spouted bed reactor. Yields and product composition. Ind Eng Chem Res 2000;39:1925–33.

[67] Li S, Xu S, Liu S, Yang C, Lu Q. Fast pyrolysis of biomass in free-fall reactor for hydrogen-rich gas. Fuel Process Technol 2004;85:1201–11.

[68] Commandré JM, Lahmidi H, Salvador S, Dupassieux N. Pyrolysis of wood at high temperature: the influence of experimental parameters on gaseous products. Fuel Process Technol 2011;92:837–44.